Optical Engineering

OpticalEngineering.SPIEDigitalLibrary.org

Momentum predictability and heat accumulation in laser-based space debris removal

Stefan Scharring
Lukas Eisert
Raoul-Amadeus Lorbeer
Hans-Albert Eckel

SPIE.

Stefan Scharring, Lukas Eisert, Raoul-Amadeus Lorbeer, Hans-Albert Eckel, "Momentum predictability and heat accumulation in laser-based space debris removal," *Opt. Eng.* **58**(1), 011004 (2019), doi: 10.1117/1.OE.58.1.011004.

Momentum predictability and heat accumulation in laser-based space debris removal

Stefan Scharring,[a,*] Lukas Eisert,[a,b] Raoul-Amadeus Lorbeer,[a] and Hans-Albert Eckel[a]
[a]German Aerospace Center (DLR), Institute of Technical Physics, Stuttgart, Germany
[b]University of Stuttgart, Institute for Applied Analysis and Numerical Simulation, Stuttgart, Germany

Abstract. Small space debris objects of even a few centimeters can cause severe damage to satellites. Powerful lasers are often proposed for pushing small debris by laser-ablative recoil toward an orbit where atmospheric burn-up yields their remediation. We analyze whether laser-ablative momentum generation is safe and reliable concerning predictability of momentum and accumulation of heat at the target. With hydrodynamic simulations on laser ablation of aluminum as the prevalent debris material, we study laser parameter dependencies of thermomechanical coupling. The results serve as configuration for raytracing-based Monte Carlo simulations on imparted momentum and heat of randomly shaped fragments within a Gaussian laser spot. Orbit modification and heating are analyzed exemplarily under repetitive laser irradiation. Short wavelengths are advantageous, yielding momentum coupling up to ~40 mNs/kJ, and thermal coupling can be minimized to 7% of the pulse energy using short-laser pulses. Random target orientation yields a momentum uncertainty of 86% and the thrust angle exhibits 40% scatter around 45 deg. Moreover, laser pointing errors at least redouble the uncertainty in momentum prediction. Due to heat accumulation of a few Kelvin per pulse, their number is restricted to allow for intermediate cooldown. Momentum scatter requires a sound collision analysis for conceivable trajectory modifications. [DOI: 10.1117/1.OE.58.1.011004]

Keywords: lasers ablation; space debris removal; momentum generation; heat accumulation; Monte Carlo simulation.

Paper 180940SS received Jun. 29, 2018; accepted for publication Aug. 16, 2018; published online Sep. 22, 2018; corrected Mar. 14, 2022.

1 Introduction

1.1 *Motivation*

When one discovers a shooting star at night, this usually means an opportunity to make a secret wish. For astronauts, this moment means that one wish has already come true: whatever could have harmed or even terminated their mission, burns up now in the atmosphere instead. Man-made space junk meanwhile poses a serious threat to any space mission—being it manned space flight or one of the numerous satellites whose usage has become part of our daily life.

It was already impressively illustrated in April 2010 how small particles may have a significant impact on modern transportation: volcanic ash from Eyjafjallajökull on Iceland posed a massive danger to aircraft engines and thus disabled any aircraft movement over Europe for several days. Likewise, following Kessler and Cour-Palais,[1] the exponentially increasing number of space debris might cause such a pollution, referred to as Kessler-syndrome, that certain Earth orbits could turn useless for space flight within only a few decades.

Research and development of laser-based detection and tracking of small-sized debris objects, i.e., in the size range down to 1 cm, is a necessary prerequisite of laser-based removal, but also has a great benefit in itself. The catalog of trajectories of debris objects contains only a few objects <10 cm, whereas most of them are undiscovered, cf. Table 1. Nevertheless, if >1 cm, debris objects typically pose a lethal threat for satellites and manned spacecraft, where no obstacle avoidance maneuver can be provided. Comparing the respective numbers of threatening objects with the number of cataloged and publicly available data, at present Space Situational Awareness resembles a weather forecast restricted on hurricanes neglecting tornadoes, which are orders of magnitude more frequent. In this regard, lasers can not only be applied for space debris monitoring, but also their scalability with respect to average power enables their usage as a tool for debris removal as well.

1.2 *Space Debris Targets*

Two elaborate models exist for the simulation of the space debris population, namely the Ordem model from the National Aeronautics and Space Administration (NASA) and the Master model from the European Space Agency (ESA).[3] Although in the Ordem model debris objects are categorized by their density, the great variety of debris objects considered in the Master model is grouped by its source of formation. This comprises fragments from explosions and collisions, sodium-potassium (NaK) droplets, slag from solid rocket motor (SRM) firing, SRM dust, multilayered insulation, paint flakes, ejecta, and clusters. According to the Master model,[4] explosions and collisions are the main source of space debris in the size range from 1 to 10 cm for the sun-synchronous orbits (SSO), where the spatial number density of debris objects >1 cm peaks at almost $10^{-6}\,\mathrm{km}^{-3}$. Hence, we focus our considerations on aluminum fragments, which constitute the most prevalent material of this object class.[5] Nevertheless, simulations for this size range might also address both fragments of other materials,

*Address all correspondence to: Stefan Scharring, E-mail: stefan.scharring@dlr.de

Table 1 Space debris statistics, taken from Ref. 2.

Debris size	Number of objects	Properties
≥1 mm	200,000,000	Possible damage to spacecraft
≥1 cm	700,000	Satellite wall penetration
≥10 cm	29,000	Spacecraft destruction
≥5 cm	16,300	Catalogued orbital data

e.g., steel, copper, phenolic/plastic, and fiberglass, as well as multilayered insulation, NaK droplets, and SRM slag.

1.3 *Laser-Based Remediation Strategies*

The orbital velocity is a crucial parameter that determines the orbital trajectory of a space asset. Correspondingly, the applied velocity increment Δv is a central figure of merit in any kind of laser-based debris removal concept. Δv is closely related to another figure of merit in this field, namely the momentum coupling coefficient c_m of laser propulsion, which is the analog to debris removal, however, with cooperative targets that are designed for the purpose of being propelled by high-power laser beams.

c_m comes with a variety of definitions of which $c_m = \Delta p/E_L$, with Δp as the imparted momentum change and E_L as the applied laser pulse energy is the most intuitive one. For our purposes, it is more practical to normalize the defining equation by the target area A_L that is cross sectional with the laser-beam yielding $\Delta v = c_m \cdot \Phi$, where Φ is the laser fluence. The strong dependencies of c_m on Φ and other parameters like pulse length τ, wavelength λ, incidence angle ϑ, and the target material give rise to a great field of studies of which some issues are treated in the following.

In laser-based debris removal, the underlying physical process is of ablative nature, i.e., based on the recoil of a small fraction of the target surface that is ablated by the incoming high-intensity laser radiation. Due to the superior beam quality of laser radiation from appropriate devices, a focal spot with <1-m in diameter can be achieved even over a distance of several hundreds of kilometers. Therefore, laser-based concepts of space debris removal have been formulated and investigated for both Earth-based as well as satellite-borne laser operations for several decades now.[6–11]

In many of those studies, the specific target geometry has been neglected though it has a significant impact on the amount and direction of the laser-induced velocity increment. Therefore, we analyzed laser-induced momentum coupling on irregularly shaped targets in our previous paper.[12] Meanwhile, also an experimental validation of those numerical calculations has been carried out with realistic, cm-sized target geometries.[13] The main outcome of our analyses was that a notable fraction of the imparted momentum can be found in the plane perpendicular to the laser-beam propagation axis, cf. Fig. 1. Since the direction of this lateral impulse component depends on the target orientation, which is typically unknown, the controllability of the removal endeavor has to be considered.

Therefore, our concern is whether those unpredictable lateral momentum components can be neglected and accordingly whether they scatter in magnitude and orientation of the thrust angle α poses a serious challenge for the reliability and safety of laser-based debris removal operations.

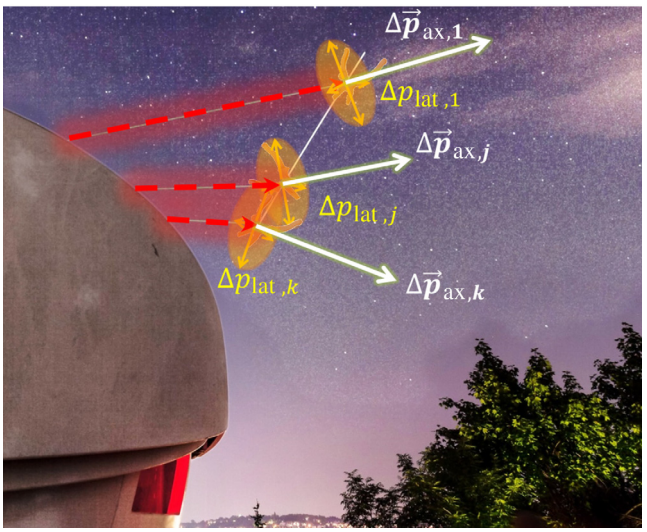

Fig. 1 Laser-induced momentum during a multiple-pulse engagement of space debris removal. During the flyover of the debris object, N laser pulses are applied from a ground-based high-energy laser station. The induced momentum components $\Delta\vec{p}_{\mathrm{ax}}$ alongside the beam propagation axis are sketched in white, whereas the plane perpendicular to the beam axis, which can be associated with lateral momentum coupling $\Delta\vec{p}_{\mathrm{lat}}$ in unpredictable direction, is highlighted in yellow. Background photo: Paul Wagner, DLR.

Moreover, recent studies have shown that the residual heat stemming from the laser ablation process is likely to rapidly heat up the debris target during repetitively pulsed laser irradiation.[14] Therefore, irradiation restrictions might apply in order to avoid target melting and compaction, which would imply the risk of losing track of the target. Hence, our studies aim to assess this secondary operational risk in laser-based removal of space debris as well.

1.4 *Scope of Work*

The paper is organized as follows: The underlying physics of laser ablation is depicted in Sec. 2.1, where both momentum generation as well as the generation of residual heat at the target are described. For the quantification of these processes, hydrodynamic (HD) simulations have been carried out, which are explained in greater detail in Sec. 3.1. Postprocessing of simulation data yields a database on thermomechanical interaction that allows for laser parameter studies on momentum coupling and residual heat, cf. Sec. 4.

Moreover, the established database serves for configuration of our simulations on laser interaction with irregularly shaped debris targets whose theoretical foundations are outlined in Sec. 2.2. The corresponding numerical implementation of this interaction is given in our raytracing-based code Expedit, which is explained in Sec. 3.2. The code allows for Monte Carlo studies on randomly generated target geometries and yields some insights on the impact of target orientation and hit accuracy, which are shown in Sec. 5.

Although Expedit, in a more simple version, was introduced earlier in our preceding paper[12] as a stand-alone program, we now present its implementation as an interaction module in a code that models orbital propagation of space assets. Therefore, some basics on orbital propagation and

orbit modification are treated in Sec. 2.3, followed by a short description of the propagator code in Sec. 3.3. In the corresponding result section (Sec. 6), we highlight first findings on single overpass engagements for the scope of space debris removal.

2 Theoretical Considerations

2.1 *Thermomechanical Coupling in Laser Ablation*

2.1.1 *Laser-ablative momentum generation*

In the concept studies on laser-based space debris removal, usually rough estimates on laser-ablative momentum coupling can be found: data on optimum impulse coupling cover a range from 14 μN/W for aluminum[10] via 75 μN/W for aluminum alloys[9] to 160 μN/W for Kevlar,[9] and sometimes are generalized covering simply one order of magnitude giving 10 to 100 μN/W for common debris materials.[11] The great variance of those data stems from the manifold dependencies of momentum coupling on both target material and laser parameters. Hence, aiming for precise simulation results, these dependencies have to be taken into account.

First of all, the threshold fluence Φ_0 for laser ablation has to be considered. Following Ref. 15, Φ_0 depends on the laser pulse length τ as follows:

$$\Phi_0 = \Delta H_{\mathrm{vs}} \cdot A_{\mathrm{opt}}^{-1} \cdot (\sqrt{D_{\mathrm{vs}} \cdot \tau} + \alpha_{\mathrm{opt}}^{-1}), \tag{1}$$

where ΔH_{vs} is the effective enthalpy of stationary evaporation, D_{vs} is the heat diffusivity in the case of stationary evaporation, A_{opt} is the target absorptivity, and the α_{opt} the optical absorption coefficient of the target. Though laser-induced momentum coupling can already be achieved below the ablation threshold, namely by photon pressure, we restrict our considerations on laser-ablative momentum coupling, which yields coupling coefficients, which are typically three to four magnitudes higher than in the case of pure photon pressure, where coupling is limited to $c_m = 6.7$ nN/W.[16]

For laser-ablative momentum coupling, Phipps introduced an elegant model to describe the dependency of c_m on material properties and laser parameters, in particular on the laser fluence.[16] Three different regimes of laser-ablative momentum coupling were found with respect to different fluence ranges: at low fluences above the ablation threshold Φ_0, momentum coupling in the so-called vaporization regime can be described according to

$$c_{m,v} = \sqrt{\frac{2(T_{\mathrm{opt}}\xi - 1)(\varrho/\alpha)\ln\xi}{\Phi_0 \cdot \xi^2}}, \tag{2}$$

where ϱ is the target density, α is the optical absorption coefficient, $\xi = \Phi/\Phi_0$ is the normalized fluence, and T_{opt} is the transmissivity.

At higher fluences, interaction of the laser pulse with already ablated material has to be considered as well: vaporized surface material rapidly expands and forms a so-called ablation jet with particle velocities that might exceed several kilometers per second. The jet is aligned to the local surface normal and exhibits a certain divergence angle, which depends on both material and laser parameters.[17,18] Hence, a fraction of the incoming laser light can be absorbed by the jet during the further temporal course of the laser pulse leading to an increase of heat and pressure inside the jet.

Above the threshold $\Phi_p = \sqrt{\tau} \times 4.79 \times 10^4$ J/cm^2, plasma ignition occurs in the ablation jet. The ionization fraction η_i, given by $\eta_i = n_i/(n_0 + n_i)$, where n_0 and n_i are the number densities of neutrals and ions, respectively, increases with the fluence yielding increasing plasma shielding of the target surface, which reduces momentum coupling. Finally, when the fluence is sufficient for a fully ionized jet, $\eta_i = 1$, this transition regime is followed by the plasma regime, where momentum coupling can be described according to

$$c_{m,p} \propto \frac{\{A/2[Z^2(Z+1)]^{1/3}\}^{9/16}/A^{1/8}}{(I\lambda\sqrt{\tau})^{1/4}}, \tag{3}$$

where A is the average atomic mass, $Z = n_e/n_i$ is the mean ionization state of the plume, and $I = \Phi/\tau$ is the average intensity of the laser pulse.

In the generalized model proposed in Ref. 16, the findings on momentum coupling for the vaporization regime and the plasma regime are joined using an interpolation, which is governed by the ionization degree of the jet:

$$c_m(\Phi) = [1 - \eta_i(\Phi)] \cdot c_{m,v}(\Phi) + \eta_i(\Phi) \cdot c_{m,p}(\Phi). \tag{4}$$

This model holds for laser pulses >10 to 100 ps. For ultrashort pulses, e.g., for photomechanical ablation processes like spallation, however, the here applied assumptions on ablation processes fail, since jet formation commences when the laser pulse is already over. Nevertheless, a similar behavior of $c_m(\Phi)$ can be found.[19]

2.1.2 *Residual heat in laser ablation*

Although the laser-induced sudden and strong increase of heat and pressure at the target surface yields vaporization and/or spallation of a part of the surface, the heat affected zone of the target surface may comprise much more material than the ablation jet itself. It can be seen from the simulation results shown in Fig. 2(a) that for the short-pulse regime the remaining target surface layers are rapidly heated to 2000 K and beyond. In contrast, rapid spallation of a comparatively large amount of surface material with ultrashort pulses yields lower initial temperatures at the surface of the remaining target. Although in the short-pulse regime ablation is mainly governed by surface vaporization of the heated material, fast heating with an ultrashort laser pulse raises a strong shock wave followed by a large rarefaction wave, which exceeds the maximum tensile strength of the material.[19] It can be seen from the discontinuities in Fig. 2(b) that material spallation occurs several times at the surface before the rarefaction wave sufficiently relaxes. Nevertheless, though frequently referred to as cold ablation, a significant amount of heat remains in the target after spallation, not to forget the secondary contribution by the thermalization of the laser-induced shock wave inside the material.

The overall amount of heat Q_{res} after ablation is usually quantified by the coefficient of residual heat η_{res} using the ratio:

$$\eta_{\mathrm{res}} = Q_{\mathrm{res}}/E_L. \tag{5}$$

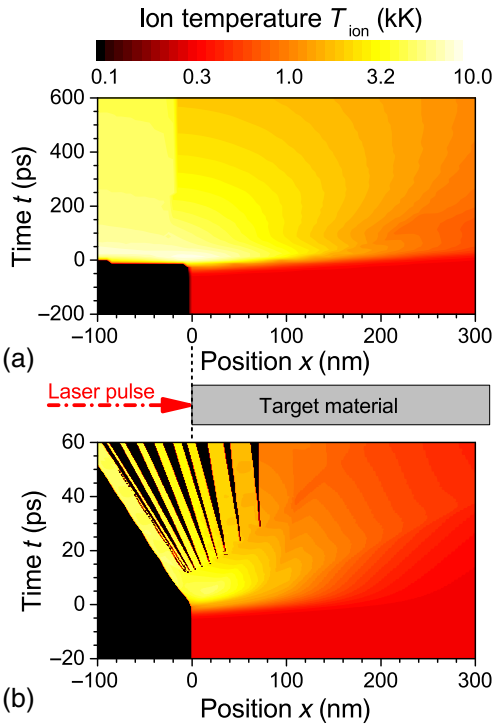

Fig. 2 Heat distribution in laser ablation with: (a) short and (b) ultrashort laser pulses. Laser parameters: $\lambda = 1064$ nm, $\vartheta = 0$ deg, (a): $\tau = 50$ ps, $\Phi = 1.49$ J/cm^2, (b): $\tau = 5$ ps, $\Phi = 0.74$ J/cm^2, results from 1-D HD simulations with Polly-2T. The target is 10- to 50-μm-thick and its surface is located at $x = 0$. The laser pulse exhibits a Gaussian temporal shape, which peaks at $t = 0$. Polly-2T is described in greater detail in Sec. 3.1.

Typical experimental data on η_{res} are 15% to 25% throughout a pulse length range from 60 fs to 6 μs, but values of up to 40% and down to 10% can be found as well.[20,21] Since this heat load per pulse contains much more energy than that expected to be reradiated from a debris during repetitive laser irradiation, heat accumulation at the target has to be considered—an effect that is already reported as a problematic issue in laser material processing,[22] where even more fortunate circumstances are usually present (convection cooling, heat sink, ultrashort laser pulses, etc.).

To account for this problem, we have introduced[14] the thermomechanical coupling coefficient c_{tm} defined by

$$c_{\mathrm{tm}}(\Phi) = \Delta p / Q_{\mathrm{res}} = c_m(\Phi)/\eta_{\mathrm{res}}(\Phi), \tag{6}$$

describing the laser-induced momentum that can be achieved, when a certain amount of residual heat can be taken into account for. Then the maximum velocity increment that can be achieved without target melting can be assessed using:

$$\Delta v_{\max} = \frac{c_m(\Phi)}{\eta_{\mathrm{res}}(\Phi)/c_p}(T_m - T_1), \tag{7}$$

where c_p is the specific heat of the target, T_1 is the initial temperature before the first-laser pulse, and T_m is the melting point.

2.2 *Thermomechanical Coupling with Irregularly Shaped Targets*

Although in the previous section, laser–matter interaction has been described in detail with respect to the laser parameters Φ, τ, and λ and material, the specific target shape has to be addressed as well since the target geometry significantly affects momentum magnitude and, in particular, its direction. A first approach has been undertaken in this regard by Liedahl et al.[23] considering that each surface element of the target exhibits a momentum component that is aligned alongside the local surface normal. For this purpose, the area-matrix concept was introduced enabling the analytical calculation of laser-imparted momentum on simple target geometries. As a drawback, however, the fluence dependency of c_m had to be neglected in that method. Therefore, we proposed an extension of the area-matrix concept taking into account for fluence variations throughout the target surface, which now requires a numerical treatment using:

$$\vec{p}_j(\vec{r}) = -c_m(\Phi_L, \vartheta) \cdot \Phi_L(\vec{r}) \cdot dA_j(\vec{r}) \cdot \cos\,\vartheta_j(\vec{r}) d\hat{n}_j(\vec{r}), \tag{8}$$

where $\vec{p}_j(\vec{r})$ denotes the momentum induced at the position $\vec{r}$ on the j'th irradiated surface element dA_j with the local surface normal $\hat{n}_j$.[12] ϑ_j is the local incidence angle of the incoming laser beam, given by a fluence distribution $\Phi_L(\vec{r})$. Correspondingly, this approach can be extended for residual heat using:

$$dQ_j(\vec{r}) = \eta_{\mathrm{res}}(\Phi_L, \vartheta) \cdot \Phi_L(\vec{r}) \cdot dA_j(\vec{r}) \cdot \cos\,\vartheta_j(\vec{r}). \tag{9}$$

Overall momentum coupling to the target as well as acquired heat can be obtained easily by summation over all nonshadowed surface elements, $\vec{p} = \sum_j \vec{p}_j$ and $Q_{\mathrm{res}} = \sum_j dQ_j$, respectively. For comparison with momentum coupling in one-dimensional (1-D) calculations, a combined efficiency η_c was introduced by Phipps et al.[9] taking into account for the effects of "improper thrust direction on the target, target shape effects, tumbling, and so on:"

$$\Delta v_{\mathrm{ax}} = \eta_c \cdot c_m \Phi_L / \mu, \tag{10}$$

where Δv_{ax} is the velocity increment alongside the laser propagation axis and μ is the target areal mass density assessing $\eta_c \approx 30\%$.

The target areal mass density is given by $\mu = m/A_x$, where m is the target mass and A_x is the target cross-sectional area. Though not clearly stated in Ref. 9, it should be noted that A_x is usually not identical with the cross-sectional area of the target with the laser beam but defined by the characteristic length L_c of the target using[24] $A_x \approx 0.56 \cdot L_c^2$ for fragmentation debris with a characteristic length exceeding 1.7 mm, following the NASA standard breakup model (SBM). L_c, in turn, is given by the arithmetic mean of the characteristic dimensions X, Y, and Z, which are the orthogonal set of the respective maximum target extensions.[5]

2.3 *Orbit Modification by Laser-Induced Momentum*

Applying a velocity increment Δv to an orbital asset yields a modification of its trajectory. A detailed analytical treatment is given in Ref. 25 showing that, although an instantaneous altitude increase might occur, the orbital eccentricity is

raised such that the target's perigee is decreased. Typically, a Δv of 150 m/s is reported to be sufficient for perigee lowering from low Earth orbit (LEO) down to $x_p = 200$ km causing debris removal by burn-up in the upper atmosphere.[25]

With respect to multipulse irradiation of irregularly shaped debris targets, lateral impulse components have to be considered, cf. Fig. 1. In our previous work, we have shown that the irregularity of the target shape easily yields laser-induced rotation, which, due to the typically missing synchronicity of rotation and pulsed laser irradiation, leads into a chaotically spinning behavior of the object.[12] Given an arbitrary target orientation, however, evenly distributed lateral momentum components in arbitrary directions might nearly average out for a great number of laser pulses during the removal engagement.

With this simplification, the findings on average axial momentum coupling $\langle p_{\mathrm{ax}} \rangle$ can be employed for a reliable prediction of the overall imparted momentum $\Delta\vec{p}$ and hence the modified debris trajectory using

$$\Delta\vec{p} \approx \sum_{i=1}^{N} \vec{p}_{\mathrm{ax},i} \approx \langle p_{\mathrm{ax}} \rangle \times \sum_{i=1}^{N} \hat{n}_i, \tag{11}$$

where $\hat{n}_i$ is the unit vector pointing in the laser propagation direction at the i'th laser pulse. The simple product in Eq. 11 suggests that two important fields of laser-based debris removal can be optimized independently: First, laser–matter interaction, given by $\langle p_{\mathrm{ax}} \rangle$, and second, the strategy of pulsed debris irradiation as represented by $\sum_{i=1}^{N} \hat{n}_i$. Although interaction is determined by the laser configuration, the irradiation strategy can be considered independently with respect to the orbital parameters, e.g., maximum elevation $\beta_{\max}$ from the laser station, orbit altitude z and orbital eccentricity ε, and the suitable engagement interval $[\beta_{\mathrm{in}}, \beta_{\mathrm{out}}]$.

Thanks to laser-based debris monitoring techniques, which already exhibit a great precision in orbit determination,[26] the term related to the irradiation strategy in Eq. 11 is accessible by the optical measurement of both azimuthal angle φ and elevation angle β during the overfly, i.e., $\hat{n}(t) = [\cos\beta(t) \cdot \cos\varphi(t), \cos\beta(t) \cdot \sin\varphi(t), \sin\beta(t)]$ can be directly derived from laser-based measurements.

3 Methods

3.1 *Hydrodynamic Simulations on Thermomechanical Coupling*

In order to derive the dependencies of thermomechanical coupling from the laser pulse parameters, HD simulations have been carried out with the 1-D code Polly-2T, provided from M. Povarnitsyn at the Joint Institute for High Temperatures at the Russian Academy of Sciences, Moscow. In Polly-2T, the target material is simulated using semiempirical equations of state for ion lattice and electron gas taking also into account for metastable states. Laser-beam coupling into the target is modeled with the Helmholtz equation. Heat distribution within the material is calculated using the two-temperature model. Interaction of the laser radiation with the induced material response is in particular accounted for by the usage of dynamic models for dielectric permittivity, heat conductivity in the electron gas and electron–phonon coupling, which cover a great range of electron temperatures.[27] A detailed description of the HD code is given in Ref. 28.

Postprocessing of HD simulation results comprises the calculation of imparted momentum in laser ablation yielding c_m for the chosen laser parameter set of $\Phi, \tau, \lambda, \vartheta$ and polarization. A corresponding laser parameter study with corresponding details is described in Ref. 19.

For the scope of our study, the calculation of residual heat was added to simulation postprocessing. Therefore, the temporal course of additional thermal energy after ablation was derived and the course of additional kinetic energy was analyzed with respect to imparted recoil and kinetic energy associated with shock wave formation. The latter fraction was added to the increase of thermal energy since thermal relaxation of the shock wave can be assumed. An approximation was undertaken to estimate the boundary value of residual heat from the ablation event. The results of the simulations are analyzed in Sec. 4.

3.2 *Simulation of Laser Interaction with Irregularly Shaped Targets*

Expedit is a code written in C++ for the calculation of laser–matter interaction with arbitrarily shaped targets. Targets are given as sets of finite surface elements and interaction with the discretized laser beam is calculated for each ray-surface intersection, provided no self-shadowing occurs. This method enables to attribute a specific fluence $\Phi(\vec{r})$ to each ray and, hence, to derive a fluence-specific imparted momentum $\Delta p[\Phi(\vec{r})]$ to each surface element, cf. Eq. 8. In this regard, fit functions describing $c_m(\Phi)$ are taken from Polly-2T results and used for configuration of Expedit. The initial version of Expedit is described in greater detail in Ref. 12, an experimental validation can be found in Ref. 13.

Expedit was recently rewritten and upgraded during the seconds author's thesis.[29] This upgrade comprises the implementation of Expedit on a graphics processing unit using Cuda and, for raytracing operations, NVidia Optix. Hence, the code is massively parallelized using 3840 cores (NVidia Quadro P6000), which yields a great performance increase compared to Ref. 12. Moreover, a discretized calculation of residual heat following Eq. 9 was implemented as well and code-wrapping allows user-friendly employment via a Python scripting. The results of our recent studies with the Expedit module are reported in Sec. 5.

3.3 *Orbital Propagation of Space Objects*

For calculation of the orbital propagation of the space debris target, a Python script was written using a Newtonian approach, i.e., taking only into account for the Earth's gravitational field but neglecting secondary factors such as atmospheric drag, radiation pressure, solar, and lunar gravitation. The propagator is initialized with the target's position $\vec{x}$ and velocity $\vec{v}$ at a certain point in time. Then $\vec{x}$ and $\vec{v}$ are propagated considering gravitational acceleration via the velocity verlet algorithm with a time step size of $\Delta t = 100$ ms as described in detail in Ref. 29.

Propagator initialization can be done by choosing a circular orbit at a certain altitude over a specific location on Earth. Moreover, it is possible as well to use orbital datasets in the two-line-element format. Additionally, the target's orientation is specified with propagator initialization. Target rotation can be propagated as well, but this feature is not

used in the work presented here. Instead, random orientation of the target before each laser pulse is chosen.

The propagator calls Expedit as a laser–matter interaction module each time a laser pulse is initiated. The Expedit module returns the corresponding increments of translational and rotational momentum Δp and ΔL, respectively, which are considered for further orbital propagation of the target. The respective simulation results on multipulse irradiation of space debris are shown in Sec. 6.

4 Laser–Matter Interaction Database

In general, solid-state lasers with short pulses are proposed for debris removal. It can be seen from Table 2 that in the case of ground-based debris removal, the range of recommended laser parameters is rather fixed. The laser wavelength is in the visible or near-infrared part of the spectrum, which can be ascribed to both atmospheric transmittance as well as the availability of suitable high-energy laser sources. In contrast, for space-based laser operation, shorter wavelengths are easily possible.

For the pulse length, a similar issue applies. The propagation of short high-energy laser pulses is again limited by the Earth's atmosphere, namely by air breakdown at high intensities. For space-based operation, much shorter pulse lengths down to femtoseconds are easily conceivable, cf. Table 2. In turn, due to the lower ablation threshold which scales with $\sqrt{\tau}$, less pulse energy is needed.

Since aluminum appears to be a rather prevalent material in small-sized space debris,[30] it constitutes a good starting point for our considerations on laser–matter interaction. Following the proposals from the literature in Table 2, we performed a laser parameter study, using Polly-2T for laser–matter interaction with aluminum targets. Our study covers the wavelength range of $\lambda = 248$ nm to 1.536 μm, pulse lengths from $\tau = 100$ ps to 10 ns and fluences starting from $\Phi = 0.1$ J/cm^2 up to 100 J/cm^2. A detailed description on their analysis is given in Ref. 19.

4.1 *Momentum Coupling*

Results on momentum coupling obtained from simulation postprocessing are depicted in Fig. 3. $c_m(\Phi)$ shows the typical behavior of onset of momentum coupling at Φ_0, rapid increase of c_m in the vaporization regime in junction with a slight decrease in the transition regime until the decrease of c_m dominates for higher fluences due to plasma shielding. For the usage in our simulations on debris removal and for the scope of a quantitative analysis on momentum coupling, the fluence dependency of the simulation results was fitted using:[13]

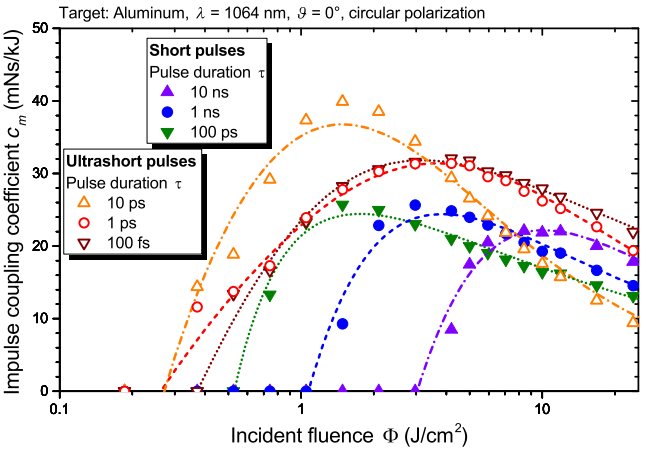

Fig. 3 Momentum coupling with aluminum targets at $\lambda = 1064$ nm for various laser pulse lengths. Results from 1-D HD simulations with Polly-2T.

$$c_m(\Phi) \approx \frac{\Phi - \Phi_0}{\Delta\Phi + (\Phi - \Phi_0)} \cdot b \cdot 12.46 \cdot A^{7/16} \cdot \left(\frac{\sqrt{\tau}}{\lambda \cdot \Phi}\right)^c . \tag{12}$$

which is valid for $\Phi \geq \Phi_0$, whereas $c_m(\Phi < \Phi_0) = 0$. Note that in Eq. 12 Φ is given in J/cm^2. For wavelength λ and pulse length τ, however, the usual SI units are used (m and s, respectively).

The fit function in Eq. 12 exhibits four free parameters $\Phi_0, \Delta\Phi, b, c$ and was deduced from Eq. 4 neglecting the vaporization regime since in our simulations the thresholds for material ablation Φ_0 and plasma ignition Φ_p were found to be rather similar. Assuming for simplification that $\eta_i \propto \Phi$, the transition regime can be characterized by the transition fluence Φ_t, where half of the jet is ionized, $\eta_i = 0.5$, which occurs at $\Phi_t = \Phi_0 + \Delta\Phi$. In practical terms, the transition range $\Delta\Phi$ is more or less related to the position Φ_{opt} of the curve maximum, whereas the peak parameter b describes the maximum value of momentum coupling $c_{m,\text{opt}}$, and the plasma exponent c gives the negative slope of c_m in a log–log plot against the fluence Φ.

Table 2 Literature suggestions on laser configurations for removal of space debris in the size range of 1 to 10 cm: pulse energy E_L, pulse repetition rate f_{rep}, pulse duration τ, laser wavelength λ, and spot diameter d_s at the target's position.

Concept	Type	E_L (kJ)	f_{rep} (Hz)	τ (ns)	λ (nm)	d_s (cm)
ORION[7]	Ground-based	20	1	40	530	40
CLEANSPACE[8,31]	Ground-based	>10	>10	5 to 50	≈1000	≥60
LODR[9]	Ground-based	8.5	13	5	1060	31
LODR[9]	Space-borne	2	33	0.1	260	23
L'Adroit[32]	Space-borne	0.38	56	0.1	355	22
ICAN[11]	Space-borne	0.001 to 0.1	1000 to 90,000	1×10^{-6} to 1	1000	1 to 10

Table 3 Fit parameters and corrected regression coefficient R^2 for momentum coupling, results from HD simulations with Polly-2T on laser ablation of aluminum at $\lambda = 1064$ nm. For the atomic mass, $A = 26.98$ was used.

τ (ns)	Φ_0 (J/cm^2)	$\Delta\Phi$ (J/cm^2)	b (N/MW)	c	R^2
1×10^{-4}	0.37 ± 0.01	1.03 ± 0.24	1.696 ± 0.299	0.304 ± 0.045	0.981
1×10^{-3}	0.26 ± 0.01	4.61 ± 1.80	3.267 ± 1.098	0.621 ± 0.085	0.979
0.01	0.27 ± 0.01	2.24 ± 1.28	1.145 ± 0.310	0.793 ± 0.134	0.970
0.1	0.53 ± 0.01	0.39 ± 0.06	0.343 ± 0.006	0.344 ± 0.020	0.980
1	1.07 ± 0.03	1.43 ± 0.37	0.266 ± 0.010	0.474 ± 0.051	0.959
10	3.03 ± 0.08	4.92 ± 1.96	0.195 ± 0.015	0.583 ± 0.102	0.953

Selected results on fit parameters $\Phi_0, \Delta\Phi, b, c$ are shown in Table 3. These data allow for an assessment of laser parameter optimization in space debris removal: with respect to the minimum required fluence, Φ_0 gives an estimate for the laser pulse energy needed at a given laser spot size at the debris position. As it can be expected from Eq. 1, Φ_0 increases with τ, furthermore, for ultrashort pulses, i.e., below $\tau = 50$ ps in the case of aluminum,[19] Φ_0 stays more or less constantly on a rather low value.

For high fluences, it can be seen from the plasma exponent c that the strength of plasma shielding is significantly pronounced with greater pulse lengths, which is likely due to the longer interaction time of the expanding plume with the ongoing laser pulse. The high data for c in the picosecond range, however, are somewhat misleading here since in the absence of plasma shielding for ultrashort pulses c_m is limited by the maximum tensile strength of the material.[19] Overall, the plasma exponent c is considerably higher than the theoretical value of 1/4 derived from Phipps, cf. Eq. 3. This can be ascribed to the simplification realized in our fitting function, Eq. 12, which neglects the fluence dependency of the mean ionization state $Z = Z(\Phi)$ in Eq. 3.

The fluence Φ_{opt} for optimum impulse coupling can be obtained using:

$$\Phi_{\text{opt}} = \Phi_0 + (1/c - 1)\Delta\Phi/2 + q, \tag{13}$$

with the parameter q defined as

$$q = \sqrt{\Delta\Phi[\Phi_0/c + \Delta\Phi/(4c^2) + \Delta\Phi/4 - \Delta\Phi/(2c)]}. \tag{14}$$

Then $c_{m,\text{opt}}$ can be derived using Eq. 12, cf. Fig. 4. Simulation results show a clear increase of momentum coupling with decreasing wavelength, which corresponds to the increasing absorptivity in this case. Basically, this trend is confirmed by experimental data where ablation by visible laser light yields approximately twice as much momentum or even more than in the near-infrared. A specific dependency of $c_{m,\text{opt}}$ on the pulse length is not clearly pronounced.

Summing up, in terms of momentum coupling, short-laser pulses at a short wavelength seem to be advisable from a theoretical point of view. Nevertheless, the pulse length specific technological challenge to achieve the desired pulse energy has to be taken into account as well as, if a ground-based technology is chosen, high-intensity pulse propagation through the atmosphere.

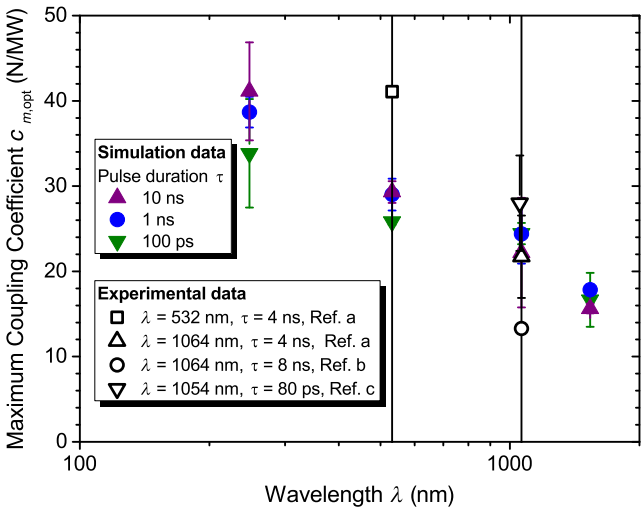

Fig. 4 Optimum laser-ablative momentum coupling of aluminum, results from 1-D HD simulations with Polly-2T in comparison with experimental data. References for experimental data: a: Ref. 33, b: Ref. 34, and c: Ref. 35, respectively.

4.2 *Thermal Coupling*

Although in the past laser parameter studies often focused on the maximization of c_m as the core figure of merit in laser-propulsive issues, recent considerations on the accumulation of residual heat from laser ablation gave rise to the usage of an alternative metric for laser parameter optimization.[14]

Similar to the treatment of our c_m data from HD simulations, the results on the residual heat η_{res} in laser ablation, which are depicted elsewhere[35] were approximated using the following empirical function:

$$\eta_{\text{res}}(\Phi) = \frac{a_0 + a_1\Phi + a_2\Phi^2}{1 + a_3\Phi + a_4\Phi^2 + a_5\Phi^3} (\Phi > 0) \tag{15}$$

yielding the fit parameters a_{0-5} depicted in Table 4. The enumerator of Eq. 15 describes, roughly speaking, the course of $\eta_{\text{res}}(\Phi)$ in the regime of heating and melting below Φ_0, whereas the denominator more or less takes into account for $\eta_{\text{res}}(\Phi)$ in the ablation regime. For short-laser pulses

Table 4 Fit parameters for residual heat $\eta_{\mathrm{res}}(\Phi)$ at $\lambda = 1064$ nm, results from HD simulations with Polly-2T on laser ablation of aluminum.

τ (ns)	a_0	a_1 (J^{-1} cm^2)	a_2 (J^{-2} cm^4)	a_3 (J^{-1} cm^2)	a_4 (J^{-2} cm^4)	a_5 (J^{-3} cm^6)	R^2
1×10^{-4}	0.072 ± 0.005	-0.09 ± 0.02	0.036 ± 0.011	-1.12 ± 0.34	0.48 ± 0.20	0.013 ± 0.006	0.696
1×10^{-3}	0.071 ± 0.003	-0.09 ± 0.01	0.035 ± 0.007	-1.18 ± 0.22	0.46 ± 0.14	0.018 ± 0.005	0.844
0.01	0.058 ± 0.005	-0.12 ± 0.02	0.070 ± 0.024	-1.74 ± 0.25	0.82 ± 0.25	0.136 ± 0.057	0.936
0.1	0.067 ± 0.004	-0.16 ± 0.03	0.320 ± 0.048	-2.38 ± 0.12	2.11 ± 0.13	0.607 ± 0.122	0.997
1	0.067 ± 0.005	-0.09 ± 0.02	0.055 ± 0.012	-1.15 ± 0.05	0.35 ± 0.03	0.059 ± 0.021	0.988
10	0.063 ± 0.003	-0.03 ± 0.01	0.010 ± 0.004	-0.46 ± 0.02	0.07 ± 0.01	0.003 ± 0.003	0.999

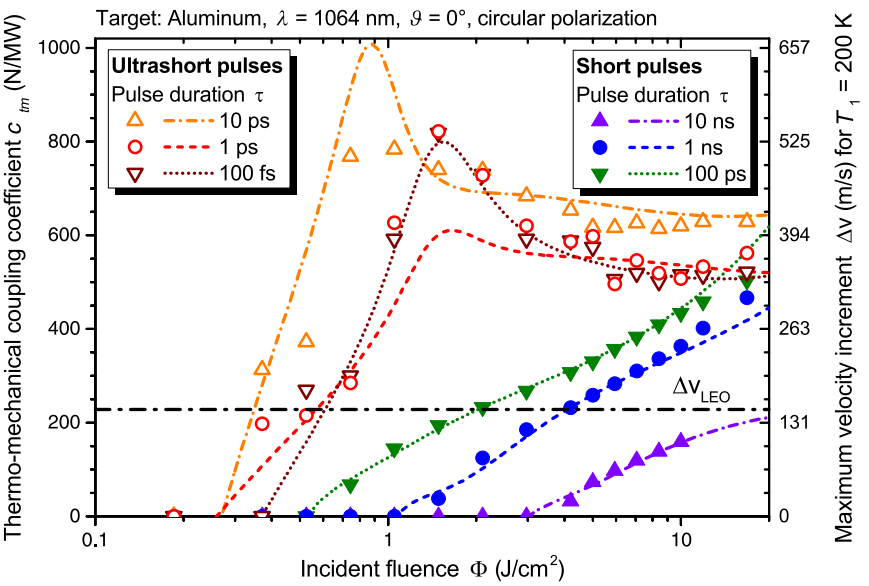

Fig. 5 Dependency of thermomechanical coupling from laser parameters. Results from HD simulations with Polly-2T on laser ablation of aluminum at $\lambda = 1064$ nm wavelength, circular polarization, and perpendicular beam incidence. Note that solid lines do not represent fitting curves of $c_{\mathrm{tm}}(\Phi)$ here but have merely derived from Eq. 6 using the tabulated fit parameters for Eq. 12 and Eq. 15, respectively.

η_{res} amounts to 20% and more around the onset of ablation and shows a slow but continuous decrease with increasing fluence. In contrast, η_{res} does not exceed 7% for ablation with ultrashort pulses. Below the ablation threshold, η_{res} equals more or less its peak value in the case of ultrashort pulses, whereas for short pulses a continuous increase of η_{res} with increasing fluence can be found.

Albeit restricted on results from simulations and aluminum as a target material, the fit parameter data from Tables 3 and 4 allow to depict the usage of the thermomechanical coupling coefficient $c_{\mathrm{tm}} = c_m/\eta_{\mathrm{res}}$ as a new metrics for laser parameter optimization in laser-ablative propulsion issues. It can be seen from Fig. 5 that ultrashort laser pulses clearly outperform short pulses, i.e., ultrashort pulses are more likely than longer pulses to achieve the required velocity increment Δv in debris removal without heating the target too much. Their superior performance in thermomechanical coupling compared to laser pulses of 100 ps and longer can mainly be attributed to their significantly lower thermal coupling cf. Sec. 2.1.2 and Ref. 35.

In contrast, for the short-pulse regime, the strong limitation in Δv without target cooldown is mirrored at the secondary y-axis of Fig. 5, cf. Eq. 7. In particular, debris removal in a single-laser station overpass does not seem to be feasible since the required velocity increment of $\Delta v_{\mathrm{LEO}} = 150$ m/s can hardly be achieved without intermediate target cooldown for laser pulses in the nanosecond range. This contradicts earlier removal concepts within a single transit using high-power laser systems in the nanosecond range, cf. Table 2. Nevertheless, validation of our findings by experimental data for various relevant debris materials is needed.

5 Interaction with Space Debris Targets

As a baseline setup for our studies on interaction with debris targets, we chose a laser configuration proposed in Ref. 8, which is a ground-based high-energy laser with $E_L = 25$ kJ, $\tau = 10$ ns, and $\lambda = 1064$ nm. With $d_s = 2/3$ m, referring to the Φ_{max}/e^2 of the Gaussian beam profile, an average fluence $\langle\Phi\rangle = 7.2$ J/cm^2 can be achieved at the target position.

As simulation targets, with the lack of available experimental or real-world data, we randomly generated 100 ellipsoids with characteristic dimensions X, Y, Z under the constraints $X/Y \in [1,2]$, $Y/Z \in [1.5, 60.3]$, $Z \in [0.3\ \text{mm}, 5\ \text{cm}]$, $A_x/m \in [0.1\ \text{m}^2/\text{kg}, 0.2\ \text{m}^2/\text{kg}]$, and $L_c \in [0.01\ \text{m}, 0.1\ \text{m}]$. These ratios are characteristic for debris fragments from ground-based satellite crash tests reported in Refs. 5 and 36, respectively, and their consideration allows for an approximate calculation of laser-target cross-sectional area and momentum directionality in our studies. However, the ellipsoid shape is still a simplified geometry and does not take into account for the potential multitude of debris shapes that might be found in this size range. This issue has to be subject to future studies.

Although A_x/m depends on L_c in the SBM, we have used equally distributed random functions for the sake of simplicity, which is justified by the large scatter in the SBM. For target generation, a Python script was used initiating target generation with random values for X/Y and Y/Z and Z, respectively, under the above-mentioned constraints. If the corresponding ellipsoid specified by X, Y, and Z matched the given constraints for A_x/m and L_c, the geometry was selected for target generation resulting in a Wavefront.obj file and attribution of the material density to the target. For raytracing, a spatial resolution of 0.1 mm was used.

5.1 *Target Orientation*

For our Monte Carlo simulation, each one of the 100 different targets was placed 2000 times in the laser spot center for a single shot. Each time the target orientation was chosen randomly, whereas the target's center of mass was aligned to the laser spot center. Mean axial velocity as well as mean thrust angle between laser-beam axis and thrust vector direction were obtained by averaging over all shots for each target, as can be seen from Fig. 6.

The simulation results shown in Fig. 6 underline the validity of Eq. 10 for the axial velocity increment: The more cross-sectional area is exposed to the laser beam at a given target mass, the higher is the acquired velocity increment.

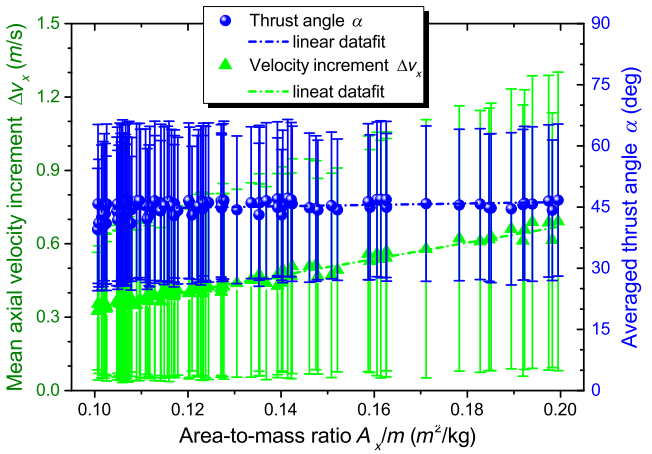

Fig. 6 Induced axial velocity increment Δv_{ax} (green data plot) as well as thrust angle α (blue plot) versus area-to-mass ratio A_x/m of 100 different flake-like aluminum targets. Each data point represents averaging from 2000 Monte Carlo samples with random orientation. The corresponding statistical errors amount to < 4% at 95% confidence level.

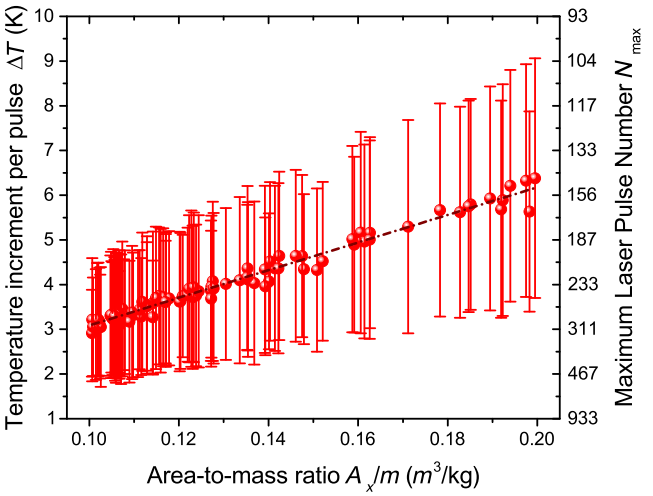

Fig. 7 Induced temperature increment ΔT per pulse versus area-to-mass ratio A_x/m of 100 different flake-like aluminum targets. The corresponding maximum laser pulse number $N_{\text{max}} = (T_m - T_1)/\Delta T$ to avoid target melting is shown as a secondary y-axis($T_1 = 0$).

In particular, it is shown here that the common definition of A_x for space debris, cf. Sec. 2.2, gives a reasonable average cross section in the case of laser irradiation as well.

In contrast, α is almost independent of A_x/m. It amounts to 45 deg $\pm$18 deg in our simulations, which implies a mean loss of efficiency in Δv_{ax} by a factor of $1 - 1/\sqrt{2}$ due to random target orientation. Lateral Δv components, however, have an unpredictable direction in the plane perpendicular to the propagation axis and might cancel out more or less during a multipulse engagement, provided the target spins rather fast.

The large scatter in α corresponds to the large scatter in Δv_{ax} depicted in Fig. 6, which is even more pronounced due to the fluence dependency of c_m with $c_m(\Phi) = c_m(\Phi_L \cos\alpha)$. Hence, the relative error $\sigma_{\Delta v_{\text{ax}}}/\langle \Delta v_{\text{ax}} \rangle$ in Δv_{ax} due to the unknown target orientation amounts to $86.3\% \pm 2.9\%$. Moreover, the relative error of Δv_{ax} due to the scatter in the target's A_x/m throughout the target ensemble is 21.4%, which is nearly identical to the scatter of A_x/m itself, cf. Eq. 10.

For laser-ablative heating a relation similar to Eq. 10 applies:[14]

$$\Delta T = c_p^{-1} \cdot \eta_{\text{res}} \Phi_L / \mu, \tag{16}$$

which is depicted in Fig. 7. Again, the greater the area exposed to the laser beam is at a given mass, the higher is the laser-induced temperature increase. The practical implication of the findings from our simulations is that the precise assessment of the target's temperature increase is strongly impeded due to missing knowledge of its orientation as well as possible uncertainties in the determination of its mass areal density μ. Hence, large safety margins have to be applied for the maximum number N_{max} of laser pulses during one transit in order to avoid target melting, cf. Fig. 7.

5.2 *Laser Pointing Accuracy*

As a next step, we introduced errors in spot positioning in our simulations. For this purpose, we varied the position of the object's center of mass for each pulse within the

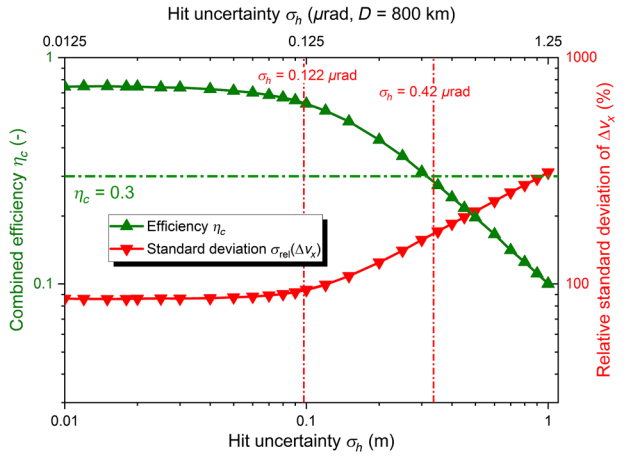

Fig. 8 Combined efficiency η_c and relative standard deviation $\sigma_{\Delta v_{ax}}/\langle \Delta v_{ax} \rangle$ of the axial velocity increment: dependency on hit uncertainty.

laser spot using a random normal distribution $N(0, \sigma_h)$, where σ_h is the hit uncertainty of the laser. For this uncertainty, we considered three parameters in a form $\sigma_h = \sqrt{\sigma_t^2 + \sigma_p^2 + \sigma_s^2}$, where σ_t is the tracking accuracy, σ_p is the pointing accuracy, and σ_s is the uncertainty due to beam wander. In Ref. 8, $\sigma_t = 0.1$ μrad and $\sigma_p = 0.07$ μrad was stated as a requirement for laser-based debris removal. In contrast, σ_s was assessed to be significantly higher in Ref. 29 amounting to roughly 0.4 μrad. Hence, we have marked the resulting value of $\sigma_h = 0.42$ μrad as orientation in our simulation result, cf. Fig. 8. The corresponding lateral uncertainty in spot positioning at a distance of 800 km (altitude of an SSO) is given there as the primary x-axis.

For the assessment of our simulation results, we calculated the combined efficiency η_c according to Eq. 10, which is depicted in Fig. 8. It should be noted here that deviating from Phipps' definition in Ref. 9, we now take into account for misalignment and the spatial distribution of the beam profile, which is both not considered there. In particular, we set $\Phi = \langle \Phi \rangle$, which in terms of the interaction process yields a overestimation of η_c if the target is located in the vicinity of the beam center, where $\Phi(0) = 2\langle \Phi \rangle$ and correspondingly an underestimation for a placement at the outer rim of the spot. Nevertheless, η_c remains a useful figure of merit in terms of technology assessment where a certain σ_h can be specified for a given spot size, distance, and pulse energy.

In the case of a very low-hit uncertainty up to ≈10 cm corresponding to the uncertainty contributions considered in Ref. 8, $\sigma_h = \sqrt{\sigma_t^2 + \sigma_p^2} = 0.122$ μrad, the combined coupling efficiency is rather constant at a level of $\eta_c \approx 0.7$. Moreover, the relative error of Δv_{ax} increases from 86%, cf. the previous section, to ≈300%, which implies a relative uncertainty due to positioning errors of up to ≈290%.

For greater hit uncertainties, which are likely when effects like uncompensated beam wander are considered as well, the momentum coupling efficiency decreases linearly with increasing σ_h, whereas the relative error in Δv_{ax} increases proportionally to σ_h. This strong performance loss in ablative momentum generation can be ascribed to the lower fluence at the outer parts of the laser spot as well as the decreasing hit rate for greater positioning uncertainties. Hence, an overall hit accuracy of ≈0.1 μrad seems to be a reasonable system requirement for the selected laser spot size.

Concerning current laser technology, pointing accuracies down to a standard deviation of 2.6 μrad have been reported[37] and currently a guide star system for turbulence compensation is designed for a residual on-sky jitter of 500 nrad rms.[38] Admittedly, these specifications do not yet match the requirements from our simulations. However, promising new technologies like Brillouin-enhanced four-wave mixing for turbulence compensation[25] and dynamic mode excitation for the control of mode instabilities[39] might yield a significant improvement of pointing stability for future ground-based laser systems. In general, however, laser system specification exhibits a greater complexity: pointing requirements would be more relaxed if a greater laser spot can be chosen. This, in turn, would require higher pulse energies in order to maintain the required fluence. In this regard, laser-beam quality, the Strehl ratio of the transmitter as well as the capability of adaptive optics to compensate beam broadening define the technological boundary conditions of in-orbit laser–matter interaction.

6 Orbit Modification under Repetitive Laser Irradiation

Though the scatter in laser-induced momentum transfer, as described in the previous section, is rather large, the overall impact to the trajectory of a space debris target has to be quantified separately, since $|\Delta \vec{p}| \ll |\vec{p}|$, which implies that in general the whole laser-debris engagement might still exhibit a satisfying reliability and controllability, i.e., safety.

Therefore, we extended the above-mentioned Monte Carlo studies attributing the debris targets to a specific trajectory passing a ground-based laser removal station taking into account the repetition rates f_{rep} and ranges of elevation β proposed in the literature.[8]

For the purpose of this study, we now restrain to a very simple target, namely a $20 \times 20 \times 1$ mm^3 aluminum plate, which has already been subject to true-scale debris removal experiments for the validation of Expedit.[13] Although the employed laser in the laboratory experiments exhibits a pulse energy of ≈80 J($\lambda = 1064$ nm, $\tau = 10$ ns), usage of a reasonable spot size at SSO requires upscaling to $E_L = 20$ kJ in our simulations. Note that such upscaled laser systems already exist and have been proposed for space debris removal.[40]

The target's orbit altitude was set at 800 km above Earth's surface with a direct transit above the ground-based laser station. The initial target temperature was set to $T_0 = 291.4$ K and 398.0 K as to the equilibrium target temperature at the beginning and the end of the sun-illuminated semiorbit, respectively. Target emissivity was set to $\varepsilon = 0.05$ according to Ref. 41.

For large distance focusing from the Earth's surface into SSO, we propose a telescope with $D_T = 8$ m diameter and a Strehl ratio of Str = 0.4 yielding $d_s = 0.7$ m when the laser-beam quality is $M^2 = 2$. We define the laser irradiation interval from a target elevation of $\beta_{in} = 30$ deg above the horizon until, shortly after station overfly, $\beta_{out} = 100$ deg is reached. We assume that the laser keeps track of the target during laser-induced orbit modification, however, with

Table 5 Predictability of debris orbital parameters after irradiation with N_p laser pulses at various repetition rates f_{rep}. Averaged results from Monte Carlo simulations for scatter of the target's position $\vec{r}_f$ directly after irradiation, perigee and apogee altitude, x_p and x_a, respectively, period T of revolution and temperature after irradiation during dawn (T_1) and dusk (T_2), respectively, initial orbit altitude: 800 km (circular).

f_{rep} (Hz)	N_p	$\sigma\vec{r}_f$ (m^3)	x_p (km)	x_a (km)	T (s)	T_1 (K)	T_2 (K)
0.1	18	$36 \times 46 \times 59$	796.9 ± 1.8	800.6 ± 0.5	6041.8 ± 1.2	338 ± 11	439 ± 10
0.2	35	$50 \times 65 \times 85$	794.1 ± 2.7	801.0 ± 0.6	6040.3 ± 1.7	375 ± 15	475 ± 14
0.5	88	$80 \times 102 \times 133$	785.4 ± 3.9	802.4 ± 0.9	6035.7 ± 2.6	487 ± 22	580 ± 21
1	175	$115 \times 147 \times 185$	771.2 ± 5.6	804.6 ± 1.2	6028.1 ± 3.7	658 ± 29	739 ± 26
2	351	n.d.	n.d.	n.d.	n.d.	$> T_m$	$> T_m$

a pointing accuracy of $\sigma_p = 0.42$ μrad, cf. Sec. 5.2. Various pulse repetition rates are tested, ranging from 0.1 to 50 Hz. For each irradiation configuration $N_s = 800$ modified trajectories with random target orientation are taken as Monte Carlo samples in order to derive the overall perigee lowering as well as temperature increase after the repetitive laser irradiation. The corresponding results are shown in Table 5.

With respect to the uncertainty of the resulting orbit parameters, it should be noted that the target orientation might have a significant effect on the efficiency of orbit modification. This is obvious when rather flat targets are assumed since the imparted momentum of a single pulse is oriented alongside the surface normal. Therefore, when the target rotation is taken into account within the simulations, the resulting perigee alterations exhibit a comparatively large scatter since the interaction of target rotation rate and pulse repetition rate might yield pulse trains with either frequent fortunate target orientations or with many detrimental target orientations.[29] In this regard, the uncertainty derived in our simulations, where the target orientation was randomly chosen for each laser pulse yields a lower scatter of orbital parameters, which might only serve as a rough estimation for the occurring uncertainties. In turn, the efficiency of a removal engagement might greatly benefit from target rotation analysis using sunlight reflectance, cf. Ref. 42. Nevertheless, the uncertainties in prediction of orbital parameters, which are associated with the scatter of our simulation results, cf. Table 5, underline the necessity of a sound covariance analysis of conceivable trajectory modifications. A corresponding collision analysis before laser operation is recommended.

It should be noted here that for LEO objects ESA requires an accuracy of orbital data yielding a 1-sigma position error <40 m $\times$ 200 m $\times$ 100 m for at least 48 h after data generation.[43] This accuracy requirement, in comparison with the uncertainty of $\vec{r}_f$, x_p, and x_a shown in Table 5, underlines the necessity of thorough postirradiation tracking of the debris particle.

With respect to thermal coupling, the results shown in Table 5 suggest that for flat targets a repetition rate of 1 Hz would be the upper limit for irradiation during one transit. For this laser configuration, however, the corresponding perigee lowering at 1 Hz is only $\Delta x_p = 28.8 \pm 5.6$ km. This perigee lowering is much too small to achieve an orbit modification yielding $x_p \approx 200$ km, which is required for target burn-up. Therefore, the main implication of thermal restrictions is that with this laser configuration it is only possible to remove debris in a series of multiple subsequent overpasses with laser irradiation and intermediate target cooldown, in contrast to the single-pass option presented for such a system as in Ref. 8.

Taking into account for pulse number restriction, it might be rather advantageous in terms of perigee lowering to choose a shorter irradiation period with a subsequently higher repetition rate. However, low-repetition rates are beneficial with respect to intraburst target cooldown, target tracking and, which is more, the required average laser power, which is considerably lower than proposed in the recent studies, cf. Table 2.

7 Conclusions and Outlook

Applying directed energy to space assets has got several implications on the motion and structural integrity of the irradiated target. Two examples, scatter of imparted momentum and accumulation of residual heat from ablation, have been studied in this paper. In this regard, our findings from simulations clarify that space debris removal by laser ablation is significantly different from simply shooting for debris with a laser like it is sometimes put forth in nonscientific media. Quite the contrary, repetitive laser irradiation during one overfly has to be limited for two reasons related to operational safety.

First, the applied momentum after laser irradiation is associated with a large uncertainty that easily might exceed its predicted average value. Sources of uncertainty are precision limitations in both pointing as well as in the determination of the target's mass areal density, possibly associated with missing knowledge of the target's material, its actual orientation and, therefore, the direction of laser-induced thrust. Though random momentum components lateral to the laser-beam propagation axis might cancel out in the long run, the orbital parameters of the debris' trajectory after irradiation can only be predicted with a remarkable uncertainty, which requires a comprehensive collision analysis in advance to laser operation.

Second, residual heat in laser ablation limits the number of possible pulses during one transit. Depending on the target material, which should remotely be reconnoitered, reasonable safety margins for laser operation should be sought in order to avoid target melting, which would turn debris removal operations into a debris compactor. Beneficially, these thermal issues suggest to operate with an average laser power that is considerably lower than known from earlier concepts.

Though under these boundary conditions high-energy lasers might not appear as a safe tool for delicate in-space operations, it does not require much more than reasonable diligence and the adequate precision of a typical scientific challenge to softly remove debris from orbit. However, in contrast to our previous paper where we compared debris removal with an orbital sweeping broom,[12] the findings from this study suggest that removal rather resembles medical surgery using a sharp scalpel.

Disclosures

We declare to have no conflicts of interest related to this work.

Acknowledgments

The authors gratefully acknowledge the scientific contribution of Claude Phipps, Jascha Wilken, Jens Rodmann, Michael Zwilich, and Daniel Burandt in inspiring discussions. We especially thank Mikhail Povarnitsyn for providing us with the Polly-2T code.

References

1. D. J. Kessler and B. G. Cour-Palais, "Collision frequency of artificial satellites: the creation of a debris belt," *J. Geophys. Res. Space Phys.* **83**(A6), 2637–2646 (1978).
2. C. Wiedemann and E. Stoll, "Space debris—trends and challenges," in *Presentation at DLR Stuttgart*, German (2017).
3. P. H. Krisko et al., "ORDEM 3.0 and MASTER-2009 modeled debris population comparison," *Acta Astronaut.* **113**, 204–211 (2015).
4. S. Flegel, "Maintenance of the ESA MASTER model," Final Report 21705/08/D/HK, Technical University of Braunschweig (2011).
5. P. Krisko, M. Horstman, and M. Fudge, "SOCIT4 collisional-breakup test data analysis: with shape and materials characterization," *Adv. Space Res.* **41**(7), 1138–1146 (2008).
6. W. Schall, "Orbital debris removal by laser radiation," *Acta Astronaut.* **24**, 343–351 (1991).
7. C. R. Phipps et al., "ORION: clearing near-earth space debris using a 20-kw, 530-nm, earth-based, repetitively pulsed laser," *Laser Part. Beams* **14**, 1–44 (1996).
8. B. Esmiller et al., "Space debris removal by ground-based lasers: main conclusions of the European project CLEANSPACE," *Appl. Opt.* **53**(31), I45–I54 (2014).
9. C. Phipps, "A laser-optical system to re-enter or lower low Earth orbit space debris," *Acta Astronaut.* **93**, 418–429 (2014).
10. S. Shuangyan, J. Xing, and C. Hao, "Cleaning space debris with a space-based laser system," *Chin. J. Aeronaut.* **27**(4), 805–811 (2014).
11. R. Soulard et al., "ICAN: a novel laser architecture for space debris removal," *Acta Astronaut.* **105**, 192–200 (2014).
12. S. Scharring, J. Wilken, and H.-A. Eckel, "Laser-based removal of irregularly shaped space debris," *Opt. Eng.* **56**(1), 011007 (2017).
13. R.-A. Lorbeer et al., "Experimental verification of high energy laser-generated impulse for remote laser control of space debris," *Sci. Rep.* **8**, 8453 (2018).
14. S. Scharring, R.-A. Lorbeer, and H.-A. Eckel, "Heat accumulation in laser-based removal of space debris," *AIAA J.* **56**, 2506–2508 (2018).
15. D. Baeuerle, *Laser Processing and Chemistry*, 3rd ed., Springer, Berlin (2000).
16. C. Phipps et al., "Review: laser-ablation propulsion," *J. Propul. Power* **26**, 609–637 (2010).
17. A. V. Pakhomov and D. A. Gregory, "Ablative laser propulsion: an old concept revisited," *AIAA J.* **38**(4), 725–727 (2000).
18. D. Ali, M. Z. Butt, and M. Khaleeq-ur-Rahman, "Ablation yield and angular distribution of ablated particles from laser-irradiated metals: the most fundamental determining factor," *Appl. Surface Sci.* **257**, 2854–2860 (2011).
19. S. Scharring, R.-A. Lorbeer, and H.-A. Eckel, "Numerical simulations on laser-ablative micropropulsion with short and ultrashort laser pulses," *Trans. JSASS Aerosp. Technol. Jpn.* **14**(ists30), Pb69–Pb75 (2016).
20. M. Autric, "Thermomechanical effects in laser–matter interaction," *Proc. SPIE* **3343**, 354–362 (1998).
21. A. Y. Vorobyev et al., "Residual thermal effects in Al following single ns- and fs-laser pulse ablation," *Appl. Phys. A* **82**(2), 357–362 (2006).
22. R. Weber et al., "Heat accumulation during pulsed laser materials processing," *Opt. Express* **22**(9), 11312–11324 (2014).
23. D. A. Liedahl et al., "Pulsed laser interactions with space debris: target shape effects," *Adv. Space Res.* **52**, 895–915 (2013).
24. N. L. Johnson et al., "NASA's new breakup model of Evolve 4.0," *Adv. Space Res.* **28**(9), 1377–1384 (2001).
25. C. R. Phipps et al., "Removing orbital debris with lasers," *Adv. Space Res.* **49**, 1283–1300 (2012).
26. T. Hasenohr et al., "STAR-C: towards a transportable laser ranging station," in *68th Int. Astronautical Congress (IAC)*, Adelaide, Australia, https://elib.dlr.de/116523/ (2017).
27. M. E. Povarnitsyn et al., "A wide-range model for simulation of pump-probe experiments with metals," *Appl. Surf. Sci.* **258**, 9480–9483 (2012).
28. M. E. Povarnitsyn et al., "Dynamics of thin metal foils irradiated by moderate-contrast high-intensity laser beams," *Phys. Plasmas* **19**, 023110 (2012).
29. L. Eisert, "Numerical simulations on momentum coupling and orbit modification in laser-based debris removal," Bachelor's Thesis, University of Stuttgart, https://elib.dlr.de/119400/ (2018).
30. J. N. Opiela, "A study of the material density distribution of space debris," *Adv. Space Res.* **43**, 1058–1064 (2009).
31. B. Esmiller, C. Jacquelard, and H.-A. Eckel, "CLEANSPACE—space debris removal by ground based laser—main conclusions," in *High Power Laser Ablation/Beamed Energy Propulsion, Presentation on Conf.-DVD*, Santa Fe, New Mexico (2014).
32. C. Phipps, "L'ADROIT a spaceborne ultraviolet laser system for space debris clearing," *Acta Astronaut.* **104**, 243–255 (2014).
33. B. D'Souza, "Development of impulse measurement techniques for the investigation of transient forces due to laser-induced ablation," PhD Thesis, University of Southern California (2007).
34. S. Scharring et al., "Low-noise thrust generation by laser-ablative micropropulsion," in *Int. Electric Propulsion Conf.*, Paper IEPC-2015-143/ISTS-2015-b-143, https://elib.dlr.de/97576/ (2015).
35. C. R. Phipps et al., "Laser impulse coupling measurements at 400 fs and 80 ps using the LULI facility at 1057 nm wavelength," *J. Appl. Phys.* **122**, 193103 (2017).
36. T. Hanada et al., "Outcome of recent satellite impact experiments," *Adv. Space Res.* **44**, 558–567 (2009).
37. G. Genoud et al., "Active control of the pointing of a multi-terawatt laser," *Rev. Sci. Instrum.* **82**, 033102 (2011).
38. M. Lingham et al., "Adaptive optics tracking and pushing system for space debris manoeuvre," *Proc. SPIE* **10703**, 107030O (2018).
39. H.-J. Otto et al., "Controlling mode instabilities by dynamic mode excitation with an acousto-optic deflector," *Opt. Express* **21**, 17285–17298 (2013).
40. A. M. Rubenchik, A. C. Erlandson, and D. Liedahl, "Laser system for space debris cleaning," *AIP Conf. Proc.* **1464**, 448–455 (2012).
41. D. E. Gray, *American Institute of Physics Handbook*, 3rd ed., McGraw-Hill, New York (1972).
42. B. D. Pontieu, "Database of photometric periods of artificial satellites," *Adv. Space Res.* **19**(2), 229–232 (1997).
43. H. Krag, T. Flohrer, and N. Bobrinsky, "ESA's SST activities and plans for the years 2017–2020," in *Defence Satellites, Conf. Presentation* (2016).

Stefan Scharring received his diploma degree in physics from the University of Freiburg in 2000 and his doctoral degree in aerospace engineering from the University of Stuttgart in 2013. He works as a senior scientist at the Institute of Technical Physics at the German Aerospace Center (DLR). His current research interests cover the field of laser–matter interactions and their aerospace applications, in particular for space debris monitoring and removal.

Lukas Eisert received his bachelor's degree in simulation engineering from the University of Stuttgart in 2018. For his bachelor's thesis, he investigated the orbital alternation due to laser ablation. At the moment, he is enrolled in the astronomy master's program at the University of Heidelberg. He worked as a research assistant at DLR's Institute of Technical Physics.

Raoul-Amadeus Lorbeer received his diploma degree in physics from the University of Hanover in 2007 and his doctoral degree from the same university in 2012. He is a research scientist at DLR's Institute of Technical Physics. His current research interests are focused on laser-ablative thrust generation for aerospace applications, in particular for micropropulsion and space debris removal.

Hans-Albert Eckel studied physics at the University of Kaiserslautern, Germany, where he received his doctoral degree in laser spectroscopy in 1996. He is the head of the "Impact, Protection, and Materials Program" at the DLR. Previously, he was the head of the Studies and Concepts Department at DLR's Institute of Technical Physics. There, his research focused on high-power laser sources and the assessment of future applications for laser-driven space propulsion.